Image-based feedback control for real-time sorting of microspheres in a microfluidic device†‡

Matthew S. Munson,§[a] James M. Spotts,§[b] Antti Niemistö,[bc] Jyrki Selinummi,[bc] Jason G. Kralj,[a] Marc L. Salit[a] and Adrian Ozinsky*[b]

We describe a control system to automatically distribute antibody-functionalized beads to addressable assay chambers within a PDMS microfluidic device. The system used real-time image acquisition and processing to manage the valve states required to sort beads with unit precision. The image processing component of the control system correctly counted the number of beads in 99.81% of images (2689 of 2694), with only four instances of an incorrect number of beads being sorted to an assay chamber, and one instance of inaccurately counted beads being improperly delivered to waste. Post-experimental refinement of the counting script resulted in one counting error in 2694 images of beads (99.96% accuracy). We analyzed a range of operational variables (flow pressure, bead concentration, etc.) using a statistical model to characterize those that yielded optimal sorting speed and efficiency. The integrated device was able to capture, count, and deliver beads at a rate of approximately four per minute so that bead arrays could be assembled in 32 individually addressable assay chambers for eight analytical measurements in duplicate (512 beads total) within 2.5 hours. This functionality demonstrates the successful integration of a robust control system with precision bead handling that is the enabling technology for future development of a highly multiplexed bead-based analytical device.

Introduction

Due to its unparalleled event measurement rate, flow cytometry has been the primary analytical tool for multiplexed single-cell protein analysis in routine use within biological laboratories. However, the degree of multiplexing achievable by fluorescence activated cell sorter (FACS) analysis for single-cell measurements is limited by the small number of spectrally distinct fluorophores available to label different cellular components, and the availability of antibodies that can be used in combination under the same staining conditions in fixed and permeabilized cells.[1] We recently reported the development of a microfluidic ELISA assay that uses commercially available 5.6 μm diameter beads (Luminex®) to create a protein-capture array in 4.7 nL assay chambers.[2] These beads are coded with two fluorophores to permit up to 100 simultaneous protein measurements on each sample.

Bead-based protein measurements offer a number of advantages for multiplexed protein quantification within the microfluidic regime. Because the protein capture surface area of each bead (approximately 100 μm²) is significantly smaller than that of conventional surface-based protein arrays (e.g., approximately 2000 μm² for a 50 μm diameter spot). By distributing the capture area across three dimensions, the use of beads allows higher density arrays to be created. For example, more than 55 beads can be assembled within the area of a single planar 50 μm diameter spot. By reducing the size of the protein capture array, lower volume assay chambers can be constructed—a feature that is advantageous when the number of molecules per unit volume ultimately determines ELISA sensitivity. The use of beads also avoids any requirement for the protein-capture agent to be pre-patterned onto a surface before being bonded within a microfluidic device, providing flexibility to configure the array pattern uniquely within each assay chamber.

Our previously reported device required the user to manually distribute beads into each assay chamber, a process that was slow, cumbersome, and error-prone. The fundamental challenge to scaling this assay platform was to develop an automated sorter to accurately distribute a defined number of unique bead types into individually addressable assay chambers. A particular emphasis was placed on capturing, counting, and delivering beads with single-bead accuracy. Such precision would permit the dynamic range of each measurement (a function of bead number) to be tuned for each analyte, thereby maximizing analyte capture on each bead-type without saturating the capture sites. Development of this capability would enable scaling of both the number of analytical measurements per sample and the number of independent samples that could be measured within the device.

Both open-loop and closed-loop control systems have been reported for automated microfluidic device operation across a wide spectrum of applications, including automated particle sorters.[3] Open-loop control systems, which operate without

[a]National Institute of Standards and Technology, Gaithersburg, MD, 20899, USA
[b]Institute for Systems Biology, Seattle, WA, 98103, USA. E-mail: aozinsky@systemsbiology.org
[c]Department of Signal Processing, Tampere University of Technology, FI-33101 Tampere, Finland

feedback control,[4–15] are not appropriate for our purposes because they are ill-suited to control stochastic variables. Numerous closed-loop feedback control systems have been reported for cell and bead manipulation using many types of forces, including electro-osmotic,[16–18] hydrodynamic[19–23] electrophoretic,[24] dielectrophoretic,[25] or electromagnetic.[26,27] These approaches, however, generally possess one or both of the following limitations. First, many of these systems function as selection filters, rather than discrete particle handlers, and lack the integrated capability to isolate and deliver a selected bead to a defined location. Second, several of these control methods require electrical or mechanical elements to be integrated within the device at the time of fabrication, increasing the difficulty of production and the likelihood of failure.

Here we demonstrate a closed-loop control system that incorporated image acquisition and processing feedback to execute the fluidic control steps necessary for a multilayer PDMS device[28] to sort beads with unit precision. This bead sorter, while similar to another previously reported design,[3] significantly extends the overall functionality by demonstrating: (1) single particle handling precision over thousands of duty cycles; (2) performance metrics of sorter operation, and; (3) refinement of the device design and control system software to support sustained operation without user intervention, without blockages, and without errors. We also present a statistical model of the operational parameters of the bead sorting process that has been used to evaluate the speed and efficiency of the sorter.

Experimental

Disclaimer

Certain commercial equipment, instruments, or materials are identified in this report to specify adequately the experimental procedure. Such identification does not imply recommendation or endorsement by the National Institute of Standards and Technology nor does it imply that the materials or equipment identified are necessarily the best available for the purpose.

Device design and fabrication

The device was designed using the principles described by Melin and Quake,[29] and was created using AutoCAD LT 2002 (Autodesk, San Rafael, CA) for a "push-down" valve geometry. The photolithography for the flow and control mold designs was performed by the Stanford University microfluidics foundry and the NIST Center for Nanoscale Science and Technology, respectively. The 3-layer flow mold consisted of photoresist features of the following target heights: 3 μm high SU-8 channel features (six 15 μm wide × 3 μm high bead trap channels within each of the 32 assay chambers); 15 μm high SU-8 channel features (used for the bead sorter sieve valve channels and fluidic channels between valved regions); and 16 μm high rounded channels formed from re-flowed positive photoresist for all valved regions of the device. The control mold comprised 20 μm high SU-8 features. The lithographic process is detailed in the ESI†. PDMS devices were fabricated according to standard multilayer soft lithography fabrication protocols.[28]

The control valves were actuated using 0.22 μm filtered deionized water using a pressure of 210 kPa (30 psi). Although 240 kPa (35 psi) was sufficient for the two bead sorter sieve valves (CV-33 and CV-34 in Fig. 1B), a higher pressure of 310 kPa (45 psi) was used for the reported experiments since this limited the penetration depth of the captured beads into the sieve, and facilitated subsequent bead release from the sorter. The PDMS fluidic channel network was initially passivated for 1 h with a solution containing Pluronic F-127 (Sigma, St Louis, MO) at a weight fraction of 2% in phosphate buffered saline (PBS, Invitrogen, Carlsbad, CA)[30] by blind-filling the device from the waste ports to all input control valves. The waste lines were then depressurized to atmosphere, and the primed channels were
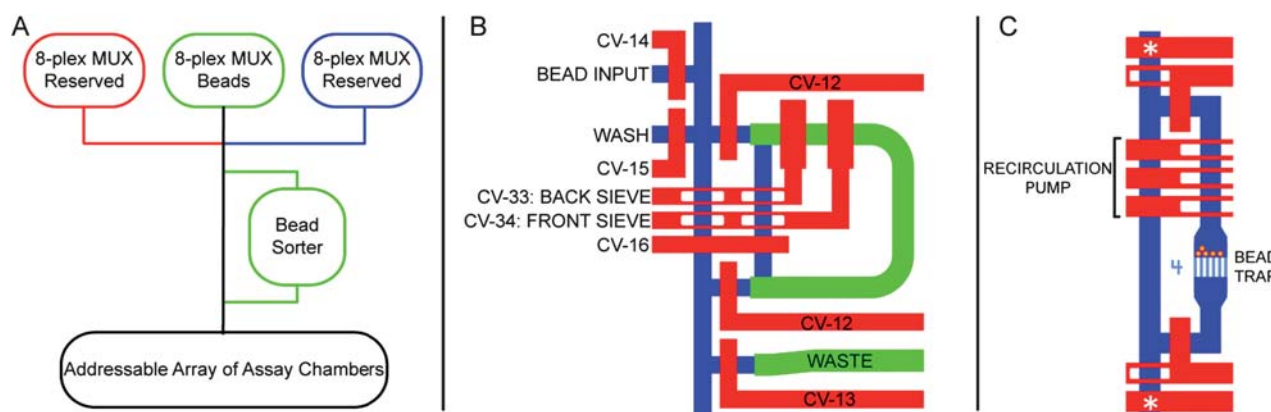
Fig. 1 Device design features for automated bead-based analytical measurements. (A) Schematic of the functional elements integrated within the device. Three independent input multiplexers converge upstream of the bead sorter. Downstream of the bead sorter is a 32-element array of individually addressable assay chambers. (B) Bead sorter fluidic network and associated control valves used for bead sorter operation. The control valve numbering scheme reflects that in the text. Control channel features and associated valves are shown in red. Rounded channels in the flow layer are shown in blue and flow channels with a square cross-sectional profile are shown in green. (C) Detailed view of one of the 32 individually addressable assay chamber loops. Each chamber incorporated a bead trap composed of six 15 μm wide × 3 μm high square profile channels (light blue) capable of capturing 5.6 μm diameter analyte-specific beads delivered by the bead sorter, as well as a 3-valve pump for recirculating the assay chamber volume. The channel volume delineated by the two control valves labelled by an asterisk (*) defines a fixed volume for precise metering of sample for subsequent analysis.

thoroughly rinsed with wash buffer (Pluronic F-127 at a weight fraction of 0.08% in PBS).

Bead solutions

To mitigate gravitational settling of the beads during loading that can cause bead density inhomogeneities to develop over time, we used a density-balanced bead loading (BL) buffer. The buffer contained glycerol at a weight fraction of 21% (Fisher Scientific, Pittsburgh, PA) in wash buffer (Pluronic F-127 at a weight fraction of 0.08% in PBS). The beads were removed from the manufacturer provided buffer by centrifugation and resuspended in BL buffer at a nominal concentration of 5×10^3 beads μL^{-1}. Further dilutions (32 fold, 16 fold, and 8 fold) of this bead stock were made using BL buffer. Actual bead concentrations were determined by manually counting beads using disposable hemacytometers. The resulting bead concentrations were (7000 ± 1000) beads μL^{-1} for the stock solution and (700 ± 300) beads μL^{-1}, (400 ± 100) beads μL^{-1}, and (200 ± 200) beads μL^{-1} for the 8, 16, and 32 fold dilutions, respectively.

Microscopy and device hardware control

All experiments were conducted on an automated microscope (Leica DMI6000B, Leica Microsystems GmbH, Wetzlar, Germany) equipped with a 40 × 0.55 NA long working distance objective. Custom filter cubes for capturing the two coding emission channels of the Luminex beads were used for all fluorescence imaging (see ESI†). Images were acquired using a 12-bit monochrome cooled CCD camera (Photometrics CoolSnap-HQ, Photometrics, Tucson, AZ). The majority of images collected utilized 2 × 2 on-chip binning to reduce image file size. The described microfluidic device was controlled as previously described.[2] Custom control software was written using LabVIEW version 8.2.1 (National Instruments, Austin, TX) for microscope and hardware control. All image processing tasks were handled using LabVIEW-embedded MATLAB scripts (The Mathworks, Natick, MA).

Results

Microfluidic device design

We designed a multiplexed bead-based analytical device that incorporated an automated, serial bead sorter (schematic, Fig. 1A). The design exploits the scaling principles intrinsic to microfluidic large-scale integration to increase the number of independent samples and bead inputs, as well as the total number of assay chambers. The device has three identical 8-plex input manifolds, one of which is dedicated to loading 8 different analyte-specific beads. Downstream of the input manifolds, a serial bead sorter (channel layout, Fig. 1B) has been incorporated to trap, enumerate, and deliver user-defined numbers of beads to a designated assay chamber. Downstream of the bead sorter is an addressable array of 32 assay chambers. Each chamber consists of a recirculation loop whose left and right sections are individually addressable (channel layout, Fig. 1C). Within the right section, a 100 μm wide gap has been added that contains a bead trap composed of six low profile channels (3 μm high by 15 μm wide). These constrictions permit fluid flow, while preventing the

passage of 5.6 μm diameter beads, thereby allowing the assembly of a bead array of arbitrary composition at the top edge. The left side of the assay chamber contains a 3 valve peristaltic pump to recirculate the contents of all 32 assay chambers in parallel. Samples can be added along the left section in a metered manner based on the channel volume defined between the isolation valves marked by asterisks.
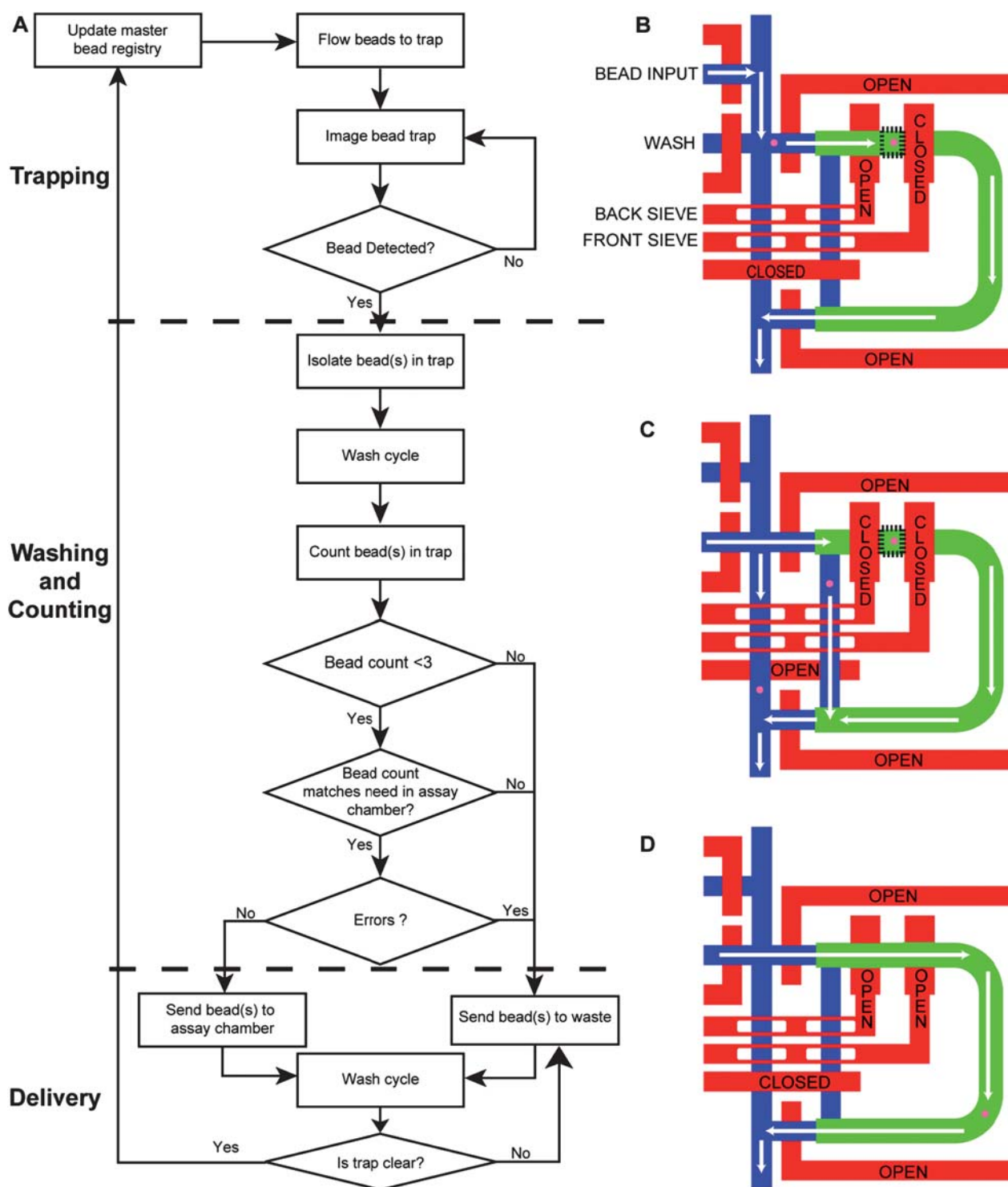
Microfluidic bead sorter operation

We designed a microfluidic device with the capability to automatically trap, count, and address beads to an assay chamber in a serial fashion. The initial design goal was to develop the capacity to load 8 beads in duplicate within 32 assay chambers (requiring 512 beads total) with single-bead accuracy. The primary emphasis was placed on developing a robust and accurate bead delivery platform, and not to maximize the bead sorting rate. The sorter design is similar to an automated cell sorter developed by others.[3] However, a key technical difference of our design was the use of sieve valves to capture beads from a flowing bead suspension.

A control logic flowchart showing the integration of image acquisition and processing steps with the fluidic control elements is presented in Fig. 2A. The corresponding fluidic control valve states are presented in Fig. 2B–D. The 125 μm × 125 μm detection region between the two sieve valves (denoted by the black dotted square in Fig. 2B) was imaged continuously using fluorescence during all phases of a sorting experiment. During the trapping phase (Fig. 2B), the bead suspension was filtered through the front sieve valve (CV-34). Detection of one or more beads in the sorter triggered the control system to advance to the wash and bead counting phase by setting the valve states as shown in Fig. 2C. Closing the back sieve valve (CV-33) after bead detection prevented additional beads from entering the detection region. Toggling from the bead suspension to the wash input in combination with opening control valve CV-16 permitted all untrapped beads to be washed out of the sorter during the five second wash phase. The final bead count was then determined using an image acquired at the end of the wash phase. Because we initially sought to load two beads of a given type per chamber, only bead capture cycles where two or fewer beads were isolated resulted in bead delivery to an assay chamber. The bead count was compared against a master registry to determine which assay chamber required that number of beads and delivery was initiated (Fig. 2D). The bead detection region was imaged continuously during the delivery step to verify that the beads exited the sorter. The delivery step proceeded in 5 s increments until the beads were determined to have exited the trap. When the control software detected that the number of beads captured was greater than the target number of beads, or if any error was encountered, the captured beads were directed to waste. This 3-phase cycle was repeated until the full complement of beads had been loaded into the assay chambers.

Bead detection algorithm

A custom MATLAB script (*trigger.m* included in the ESI†) was written to detect the arrival of beads in real time as they entered the detection region (Fig. 3A and B). Images were acquired and

Fig. 2 Microfluidic bead sorter control logic and corresponding operational valve states. Refer to Fig. 1B for valve label assignments. (A) Flowchart summarizing the control logic used to manage the three bead-sorter control states for trapping, counting, and delivering beads. The transition between fluidic valve control states within the control system architecture is delineated by the dashed lines in the flowchart. (B) During the bead trapping phase of bead sorter operation, the control valves labeled CV-12, CV-13, CV-14, and the back sieve valve (CV-33) were opened, directing the bead suspension to flow from the side input channel, through the front sieve valve (CV-34), and out to waste. The region enclosed by the dotted line between the two sieve valves was imaged continuously to detect bead arrival at the front sieve. (C) Once bead capture was detected, the control system initiated the wash and bead counting phase. The control valve states were set such that CV-12, CV-13, CV-15, and CV-16 were opened while CV-14, CV-33, and CV-34 were closed, causing wash buffer to flow from a second side input channel to remove untrapped beads upstream of the trap, after which the number of trapped beads was determined. (D) During the delivery phase both sieve valves (CV-33 and CV-34) were opened and, CV-13 and CV-16 were closed, causing wash buffer to rinse the beads from the detection region and deliver them either to waste (greater than 2) or to the addressable array (2 or fewer).
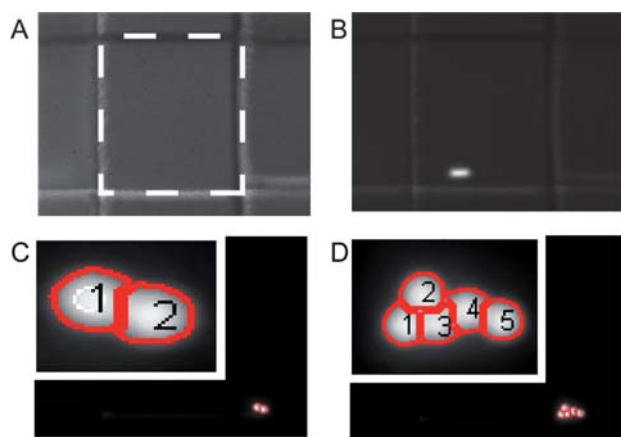
Fig. 3 Sample images acquired and analyzed by the control system during bead sorter operation. (A) Bead detection region between the two sieve valves of the bead sorter (within dotted line) was imaged continuously until (B) one or more beads were detected. (C) Segmented and counted single images for a productive cycle where 2 beads can be delivered to an assay chamber and (D) an unproductive cycle where 5 trapped beads needed to be directed to waste. Insets in (C) and (D) show enlarged views of the beads with the final segmentation and counting results overlaid. Images displayed above were auto-leveled.

analyzed every 0.6 s. First, a three pixel square median filter was applied. Beads were determined to be within the sorter if the maximum pixel intensity was more than 500 counts greater than the averaged background intensity from the first image of each sorting sequence. The value of the threshold (500 counts) was chosen because it represents twice the maximum observed variation in maximum pixel intensity between consecutive images observed over a sample of 200 background images. The triggering threshold offset was the only adjustable parameter, and was chosen conservatively to ensure that ordinary illumination intensity fluctuations did not activate the trigger. Once any pixel intensity value exceeded the threshold, the size of each high intensity region was analyzed by applying Otsu's thresholding method.[31] If at least one region with an area exceeding 50 pixels was found, the script indicated a triggering event. The triggering script successfully processed 28 079 images from the bead sorter under normal operating conditions with zero erroneous triggering events. This script required only 50 ms to process each 12 bit 696 pixel × 520 pixel image, representing only 8% of the 0.6 s total imaging frame rate during the bead trapping phase. Most of the time required per frame was dedicated to the exposure (100 ms) and data transfer.

In future work where we will sort multiple bead types containing differing amounts of the coding fluorophores, the control system software will include a look-up table of appropriate camera exposure times to insure that the fluorescence intensity from each bead type will be sufficient to activate the triggering script. The effect on image frame rate as a function of bead type also is a subject for future work.

Bead segmentation and counting algorithms

A final image acquired during the wash phase was used to determine the bead count (see Fig. 3C and D for examples) using a custom-written MATLAB segmentation and counting algorithm (*count.m* included in the ESI†). The image contrast was adjusted to span the minimum and maximum pixel intensities, and a five pixel square median filter was applied. Otsu's method[30] was then employed to threshold the image, yielding a binary image where regions of high and low fluorescence intensity were labeled foreground and background, respectively. To segment images where the fluorescence from different beads overlapped or touched, the Euclidian distance transform[31] was performed on the binary image, and a marker controlled watershed transform[32,33] was applied using the local maximum for each region as the marker. The local maxima that were used as markers were determined using the pixel values from the original image. Holes within closed contours were filled, and any region comprising less than 100 pixels was removed. Connected component labeling was used to count the number of remaining regions and the area and perimeter of each were computed. Finally, the roundness of each segmented object was calculated using eqn (1).

$$\text{Roundness} = \frac{4\pi \times \text{Area}}{\text{Perimeter}^2} \qquad (1)$$

The roundness expression has a value of 1.0 for a perfectly circular region. To derive a robust roundness threshold that reliably discriminated beads from other image features, we collected several series of test images containing different numbers of beads trapped within the sorter at, above, and below the true focal plane. Based on manual examination of the segmented test images, a roundness threshold of 0.6 was determined to be sufficient.

The time to accurately count the beads in a single image depended on the number of objects in the image. This dependence indicated that the watershed transform was the slowest component during the execution of this script. This script was executed after the 5 s wash phase and before the 5 s delivery phase to ensure that all beads in the bead detection region had sufficient time to become trapped at the sieve valve. This forced the beads into the focal plane of the microscope prior to acquiring the image passed to the counting script, which was observed to improve the accuracy of the counting script. The combined elapsed time for these two phases averaged 12.8 s in these experiments, with a standard deviation of 0.15 s. Future refinements will execute the counting script concurrently with the wash phase.

The bead segmentation and counting script incorporated four image analysis error modes that automatically directed the trapped beads to waste. Each error mode accounted for bead configurations that would likely yield an inaccurate count. In these circumstances, it was preferable to discard the beads from the ambiguous frame in order to preserve the accuracy of the constructed array. The error modes are described in detail in the ESI†. We assessed the performance of the counting script by examining 2694 images of beads. In 28 instances, image processing error modes was appropriately triggered and the captured beads were directed to waste. The accuracy of the automated counting results was compared with a visual inspection of each counted image. We identified only 5 instances of inaccurate counts across all 2694 images. One of these errors arose from the image being out of focus due to vibration of the experimental apparatus, resulting in 3 extra beads being

delivered erroneously to an assay chamber. The remaining 4 miscounts originated from the watershed transform step. When two equivalent local maxima were detected within a single bead, the watershed algorithm caused the bead to be divided into two regions that still registered above the set roundness threshold of 0.6. Three of the four miscounts of this type caused a single bead to be counted as two, resulting in one fewer bead being delivered than was accounted for in the cumulative bead count. The final miscount of this type resulted in two beads being counted as three. While this bead packet was improperly delivered to waste, this counting error had no impact on the cumulative bead count.

We explored two methods to eliminate the origin of this segmentation error, dithering and increasing the roundness threshold. The original counting script identified multiple local maxima within a single bead when there were two non-adjacent pixels with identical maximum values in the same neighborhood. Dithering the initial image eliminated this possibility (see ESI†, *ImprovedCount.m*) and corrected the counts in 4 of the 5 mis-counted images, without changing the count accuracy for images that were previously counted correctly. The second approach was to use a larger value for the roundness threshold. We found that a roundness threshold value of 0.78 was sufficient to activate an image processing error mode for all the improperly counted images. However, this higher cutoff value also caused 239 of the images that were previously counted correctly (using the 0.6 roundness threshold) to register as image processing errors, which would have caused the control program to direct the beads to waste. While providing better accuracy, this higher roundness threshold would have increased the number of beads required to produce the finished array by approximately 10%, and extended the overall sorting time by an estimated 20%.

Used together, the image processing algorithms allowed for the real-time trapping and counting of beads arriving at the sieve. An accurate bead count was computed for 99.81% of the bead capture events. In circumstances where the algorithm was not likely to give an accurate count (1.0% of counted images), an error code was recorded and the trapped objects were delivered to waste by the control system. Post-experimental refinements to the image analysis algorithms reduced the counting errors to a single instance in 2694 images of beads (99.96% accuracy).

Characterization of parameters impacting bead sorter performance

In initial experiments, we observed that the bead delivery rate declined over time due to either the input lines becoming clogged with debris or beads sedimenting in the input lines (Fig. 4A). Clog formation from debris was minimized by including an on-chip 15 µm filter for the input lines, and bead sedimentation was mitigated by suspending the beads in a density-balanced medium. After these modifications, we characterized the bead sorter performance (Fig. 4B). In these experiments, no errors in bead counting were seen, demonstrating the efficacy of the analysis algorithm. Furthermore, the observed constant rate of bead delivery over the 80 min required to perform all 4 independent sorting experiments of 64 beads each validated the success of the measures to minimize the effects of clog formation and bead sedimentation.
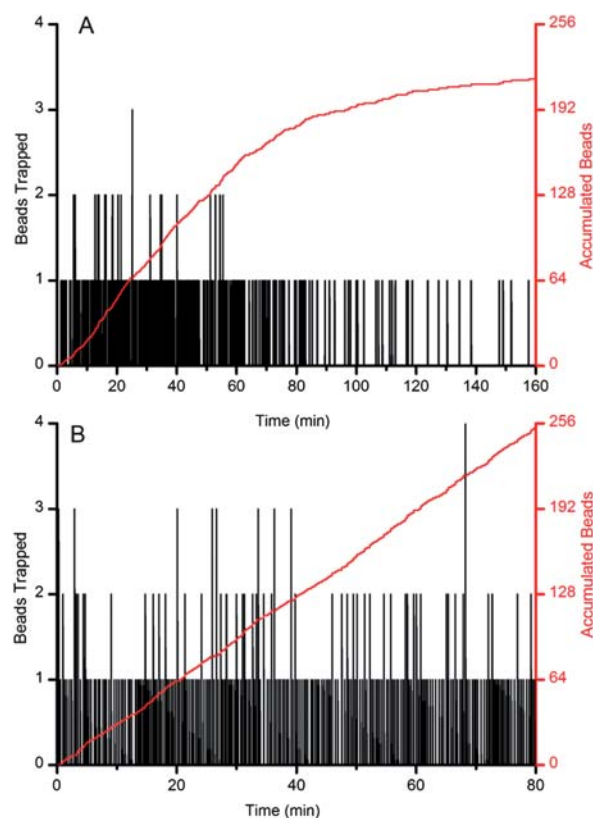
Fig. 4 Representative bead sorter performance showing the cumulative time course from four concatenated bead-sorting experiments (each to sort 32 pairs of beads). The primary *y*-axis shows the number of beads counted at the end of each wash phase. The secondary *y*-axis shows the cumulative bead count from productive sorting cycles. (A) Initial performance results showed a temporal decrease in the bead delivery rate. Factors that could contribute to this behaviour were bead sedimentation, or the formation of bead- or debris-based clogs at the channel inlet. (B) Refined bead sorter performance after a 15 µm particle filter was incorporated into the bead suspension input and the beads were suspended in a density balanced buffer. The rate of bead delivery (red line, slope of the cumulative bead curve) remained constant during each individual experiment and from experiment to experiment.

Next, we performed experiments to assess the impact of the flow rate and the bead concentration on the time per bead delivered. While the flow rate could be controlled by varying the pressure used to actuate the sieve valves, we did not systematically vary this parameter in our experiments due to the tendency of beads to become irreversibly wedged into the lower corner of the channel when the sieve was actuated at lower pressures. Instead, we examined how systematically varying both the pressure applied to the bead suspension input line and the bead concentration impacted sorter performance using flow pressures of 7 kPa, 10 kPa, 21 kPa, and 28 kPa (1 psi, 1.5 psi, 3 psi and 4 psi) in combination with bead concentrations of (700 ± 300) beads µL^{-1}, (400 ± 100) beads µL^{-1}, and (200 ± 200) beads µL^{-1}. We programmed the control software to perform four consecutive 64 bead sorts (corresponding to 2 copies of a single bead type to each of the 32 individual assay chambers) in order to characterize the time taken to deliver each bead (Fig. 5). The minimum time per bead delivered was approximately 15 s.
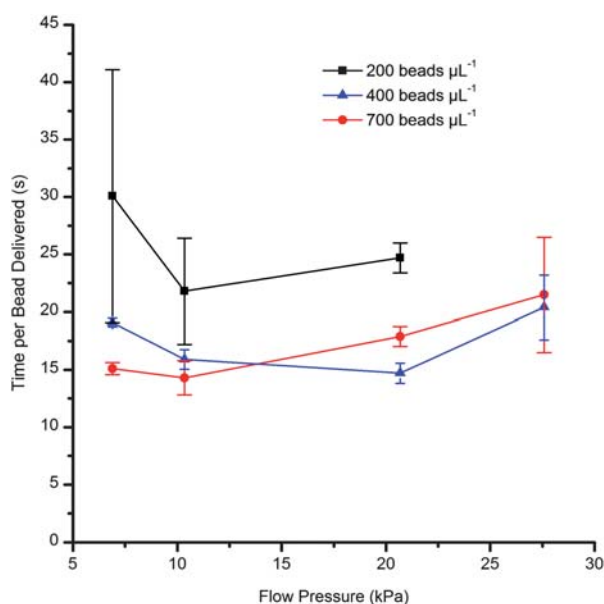
Fig. 5 The effect of inlet flow pressure applied to the bead suspension and bead concentration on the average per bead delivery time (calculated as total beads delivered divided by total sorting time). Four consecutive sorting experiments of 64 beads each were performed at the indicated inlet flow pressures and bead concentrations, and the mean time per bead delivered was determined. Error-bars indicate one standard deviation from the four repeated experiments.

Moreover, we observed that at each bead concentration the average delivery time per bead was observed to pass through a minimum with respect to the flow pressure.

We also assessed whether any of the beads processed by the sorter entered the bead detection region in aggregated form or as individual particles. We examined by eye all images collected just prior to a triggered bead capture event, and did not observe any beads to enter the trapping region as an aggregate. In 81% of the trapping events, the beads were unambiguously observed to enter the image frame as individual beads. In the remaining 19% of the trapping events, the images were inconclusive. This uncertainty arises from the unrecorded dark time between each exposure, during which time more than one bead could be trapped at the sieve valve. Examining the percentage of uncertain events for a given condition (flow rate and bead concentration) showed that the percent uncertainty was more strongly correlated with flow rate ($R^2 = 0.59$) than with bead concentration ($R^2 = 0.37$). This suggested that the uncertainty arose from the increased velocity of the beads (*i.e.*, our inability to clearly resolve them while they were moving) rather than a tendency of the beads to aggregate.

Modeling device performance

We developed a model of the bead sorter to determine if the observed delivery time could be improved by further adjustment of the key operational parameters (bead density, backing pressure, sieve valve pressure, *etc.*). The details of the model implementation can be found in the ESI†. The central assumption of the model was that the number of beads arriving at the trap would be appropriately represented by a Poisson distribution. The validity of this assumption is supported by Q–Q plots

(Fig. S2†), which provide a semi-quantitative method to assess how well the experimental data matched a theoretical Poisson distribution with the same mean.

The simulation results are shown in Fig. 6. The minimum time required per bead delivered was seen at $\lambda = 0.25$. This optimum value was anticipated to be less than 1 because the time penalty associated with not trapping a bead in a given exposure (0.6 s) was 21 times less than the time penalty associated with trapping more than two beads (12.8 s to wash beads to waste). This concept is illustrated in Fig. 6B, which shows the theoretical probability distribution of bead numbers in the bead detection region for three different values of λ (probability mass function). In Fig. 6C, the probabilities were weighted by the relative time required for the sorter to process a packet of the indicated number of beads. This graph provided a convenient method for analyzing the ratio of the productive time spent processing 1 or 2 beads relative to the wasted time spent processing empty frames or more than 2 beads. For values below the optimum, we observed that a large fraction of the time was spent waiting for the arrival of single beads, *i.e.*, the majority of time was spent processing short, but unproductive events. For values above the optimum, excess time was spent processing unusable bead numbers during a duty cycle, *i.e.*, time spent handling some number of unproductive events. The temporal efficiency (ratio of productive time to total sort time) expressed as a function of
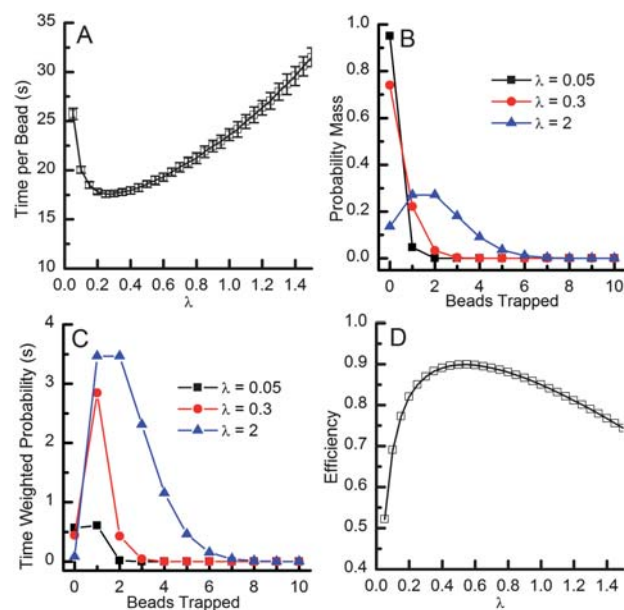
Fig. 6 Simulation to determine the optimum sorter performance. (A) The simulated time per delivered bead is plotted as a function of λ (averaged over 512 beads). The error bars are ± one standard deviation from the 100 simulations at each value of λ. A minimum time per bead of 17.6 s was found at $\lambda = 0.25$. (B) Probability mass functions for Poisson distributions with three different mean values ($\lambda = 0.05$, 0.3, and 2). (C) The probabilities shown in B are weighted by the time that would be required for the sorter to process each number of beads. This illustrates how the different duty cycles impact the distribution of time spent handling productive (1 or 2 beads) and unproductive (0 or more than 2 beads) events. (D) The temporal efficiency (ratio of useful time to total time) shown as a function of λ.

λ showed that at the minimum sort time ($\lambda = 0.25$), the temporal efficiency was 84% (Fig. 6D). While a bead distribution with $\lambda = 0.5$ had greater time efficiency (88%) than that with a $\lambda = 0.25$ distribution, the total sort time was nevertheless longer.

This model was used to gain insight into the statistical parameters governing bead sorter functionality, and revealed that optimal performance (*i.e.* the minimum total time to sort the full complement of beads) was achieved when the bead numbers being processed by the sorter at each frame of an experiment were represented by a Poisson distribution with a λ value of 0.25. This established a single quantitative metric that could be used to compare bead sorter performance under any combination of experimental variables to the best possible performance.

Comparison between model and experimental data

We calculated the best-fit Poisson distribution and its mean, λ, for each of the different sorting experiments described in Fig. 5. We then plotted the elapsed time per bead delivered as a function of λ (Fig. 7). The experimentally derived values for λ displayed good qualitative agreement with the curve predicted by the model simulations (Fig. 7A, blue overlay). We observed that several of the experimentally derived values for λ lay below those predicted by the model, and that this may reflect the observed deviations from ideal Poisson behavior as suggested by the Q–Q plots presented in Fig. S2†.

The minimum time per bead delivered correlated with an extrapolated value for λ of 0.35, in close agreement with the simulation. We also noted that several experimental conditions within the matrix of possible variables yielded close to optimal

Fig. 7 Comparison between the experimental and the modeled bead sorting performance metrics. The bead sorting data from Fig. 5 were fit to a Poisson distribution in order to determine the value of λ. The average time per bead delivered was then plotted as a function of λ. Error bars for the value of λ represent the 95% confidence limits on the fit value. The bead sorter metrics derived from the model (Fig. 6A) was overlaid for comparison.

bead sorter operation. This further indicated that the sorter operation was robust, and was not critically dependent on precise regulation of either flow pressure and or bead concentration.
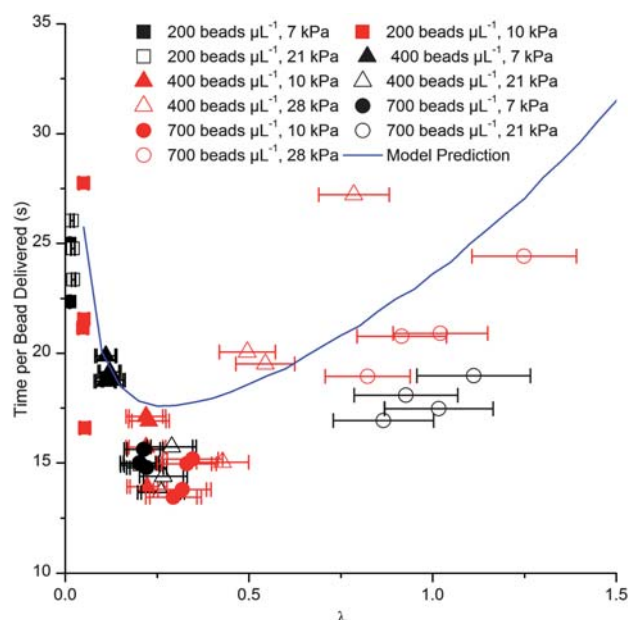
The outlying point at a concentration of 400 beads μL^{-1} and a pressure of 28 kPa deviated significantly from the other experiments at this condition due to the stochastic nature of bead arrival at the sorter. In this instance, completion of the array required a single bead, but was delayed by a series of two beads being captured and by necessity washed to waste before the final single bead was captured. Excluding this final bead capture event from the analysis yielded an average time of 22 s per bead delivered, which was comparable to that achieved in other experiments at the same conditions. Of the 43 independent sorting experiments conducted, this delay at the end of the experiment was observed once.

Discussion

Our development of a microfluidic bead sorter was motivated by the need to deliver hundreds of Luminex beads with single bead precision to <10 nL volume assay chambers to perform multiplexed sandwich-ELISA protein measurements. An automated sorter of related design has been reported previously.[3] However, that report describes the sorting of only 16 single particles, and does not address the extensibility of the approach for processing greater number of particles. Importantly, the performance metrics of this sorter are not defined. Here we have described a fully automated bead sorter that significantly extends the number of particles processed more than two orders of magnitude while achieving single bead precision over hours of processing time. Moreover, we have established performance benchmarks against which future refinements can be directly compared.

The use of sieve valves contributed to the robust performance of our sorter by permitting beads to be captured and quantified under conditions of continuous flow. This design had three advantages. First, the sorter was able to operate with faster flow rates through the bead trapping region than could be achieved by pump-driven flow, reducing the dead time prior to bead capture. Second, sieve valves permitted particles to be trapped regardless of the bead suspension flow velocity. By contrast, valve-based trap designs require that the control system respond faster than the time taken for the bead to transverse the interrogation volume. This places an upper limit on the velocity of a particle through the channel, slowing the overall sorting rate. Third, sieve valves trapped any captured bead directly against the glass surface, permitting the facile acquisition of a single, in-focus image for analysis and quantification during each duty cycle, contributing to faster sorter performance. By contrast, accurately quantifying non-spatially localized particles is slow and challenging, and requires either the collection and analysis of an image stack to accurately quantify particle numbers or the development of image analysis methods to accurately handle defocused images.

Our automated bead sorter was relatively slow, particularly in comparison to an alternative method such as stochastic particle loading. This is not a fundamental limitation for our intended application where single bead precision is paramount. The time to sort the full complement of beads (currently 2.5 h for

512 beads) can easily be accommodated during an overnight run, and permits the number of beads distributed to be further scaled at least four fold during this timeframe. While a stochastic particle distribution approach may be adequate for many applications that employ one type of particle, this approach rapidly becomes untenable as additional particle types are required for multiplexed applications.

Conclusions

We have demonstrated a fully automated closed loop control system to precisely distribute antibody-functionalized beads to addressable assay chambers within a PDMS microfluidic device. The control system used integrated image acquisition and processing as feedback to regulate the fluidic valve states, and required no additional electrical or mechanical elements to be incorporated within the device. The robustness of the sorter was shown over a range of experimental conditions that yielded performance that was close to the optimum predicted by a model of the sorter operation. While the overall speed of sorting was slow relative to FACS instrumentation, our device achieved the control necessary for sorting with single-bead accuracy, and at a speed that is appropriate for distributing antibody-coated bead sensors to perform multiplexed protein ELISA measurements within this device. Our sorter provides a robust, high-precision, and automated solution for multiplexed particle distribution whose performance far exceeds either manually operated or previously reported automated particle sorters.

Acknowledgements

Notes and references

1 K. R. Schulz, E. A. Danna, P. O. Krutzik and G. P. Nolan, *Current Protocols in Immunology*, John Wiley and Sons, Inc., 2007, ch. 8, unit 8.17.
2 A. H. Diercks, A. Ozinsky, C. L. Hansen, J. M. Spotts, D. J. Rodriguez and A. Aderem, *Anal. Biochem.*, 2009, **386**, 30–35.
3 Y. Marcy, T. Ishoey, R. S. Lasken, T. B. Stockwell, B. P. Walenz, A. L. Halpern, K. Y. Beeson, S. M. D. Goldberg and S. R. Quake, *PLoS Genet.*, 2007, **3**, 1702–1708.
4 R. J. Taylor, D. Falconnet, A. Niemisto, S. A. Ramsey, S. Prinz, I. Shmulevich, T. Galitski and C. L. Hansen, *Proc. Natl. Acad. Sci. U. S. A.*, 2009, **106**, 3758–3763.
5 S. J. Maerkl, *Integr. Biol.*, 2009, **1**, 19–29.
6 B. M. Paegel and G. F. Joyce, *PLoS Biol.*, 2008, **6**, 900–906.
7 J. Y. Wang, G. D. Sui, V. P. Mocharla, R. J. Lin, M. E. Phelps, H. C. Kolb and H. R. Tseng, *Angew. Chem., Int. Ed.*, 2006, **45**, 5276–5281.
8 B. M. Paegel, W. H. Grover, A. M. Skelley, R. A. Mathies and G. F. Joyce, *Anal. Chem.*, 2006, **78**, 7522–7527.
9 C. L. Hansen, S. Classen, J. M. Berger and S. R. Quake, *J. Am. Chem. Soc.*, 2006, **128**, 3142–3143.
10 A. J. deMello, *Nature*, 2006, **442**, 394–402.
11 D. L. L. Chen and R. F. Ismagilov, *Curr. Opin. Chem. Biol.*, 2006, **10**, 226–231.
12 B. Zheng, C. J. Gerdts and R. F. Ismagilov, *Curr. Opin. Struct. Biol.*, 2005, **15**, 548–555.
13 J. W. Song, W. Gu, N. Futai, K. A. Warner, J. E. Nor and S. Takayama, *Anal. Chem.*, 2005, **77**, 3993–3999.
14 C. L. Hansen, M. O. A. Sommer and S. R. Quake, *Proc. Natl. Acad. Sci. U. S. A.*, 2004, **101**, 14431–14436.
15 B. M. Paegel, S. H. I. Yeung and R. A. Mathies, *Anal. Chem.*, 2002, **74**, 5092–5098.
16 L. M. Fu, R. J. Yang, C. H. Lin, Y. J. Pan and G. B. Lee, *Anal. Chim. Acta*, 2004, **507**, 163–169.
17 P. S. Dittrich and P. Schwille, *Anal. Chem.*, 2003, **75**, 5767–5774.
18 A. Y. Fu, C. Spence, A. Scherer, F. H. Arnold and S. R. Quake, *Nat. Biotechnol.*, 1999, **17**, 1109–1111.
19 C. H. Chen, S. H. Cho, F. Tsai, A. Erten and Y. H. Lo, *Biomed. Microdevices*, 2009, **11**, 1223–1231.
20 R. Gomez-Sjoberg, A. A. Leyrat, D. M. Pirone, C. S. Chen and S. R. Quake, *Anal. Chem.*, 2007, **79**, 8557–8563.
21 H. W. Bang, C. N. Chung, J. K. Kim, S. H. Kim, S. Chung, J. Park, W. G. Lee, H. Yun, J. Lee, K. C. Cho, D. C. Han and J. K. Chang, *Microsyst. Technol.*, 2006, **12**, 746–753.
22 A. Wolff, I. R. Perch-Nielsen, U. D. Larsen, P. Friis, G. Goranovic, C. R. Poulsen, J. P. Kutter and P. Telleman, *Lab Chip*, 2003, **3**, 22–27.
23 A. Y. Fu, H. P. Chou, C. Spence, F. H. Arnold and S. R. Quake, *Anal. Chem.*, 2002, **74**, 2451–2457.
24 K. Takahashi, A. Hattori, I. Suzuki, T. Ichiki and K. Yasuda, *J. Nanobiotechnol.*, 2004, **2**, 5.
25 D. Holmes, M. E. Sandison, N. G. Green and H. Morgan, *IEE Proc.: Nanobiotechnol.*, 2005, **152**, 129–135.
26 R. W. Applegate, J. Squier, T. Vestad, J. Oakey, D. W. M. Marr, P. Bado, M. A. Dugan and A. A. Said, *Lab Chip*, 2006, **6**, 422–426.
27 M. M. Wang, E. Tu, D. E. Raymond, J. M. Yang, H. C. Zhang, N. Hagen, B. Dees, E. M. Mercer, A. H. Forster, I. Kariv, P. J. Marchand and W. F. Butler, *Nat. Biotechnol.*, 2005, **23**, 83–87.
28 M. A. Unger, H. P. Chou, T. Thorsen, A. Scherer and S. R. Quake, *Science*, 2000, **288**, 113–116.
29 J. Melin and S. R. Quake, *Annu. Rev. Biophys. Biomol. Struct.*, 2007, **36**, 213–231.
30 V. N. Luk and A. R. Wheeler, *Anal. Chem.*, 2009, **81**, 4524–4530.
31 N. Otsu, *IEEE Transactions on Systems Man and Cybernetics*, 1979, **9**, 62–66.
32 H. Digabel and C. Lantuejoul, *Proceedings of the International Workshop on Image Processing: Real-Time and Motion Detection/Estimation, Rennes, France*, 1979.
33 S. Beucher and C. Lantuejoul, *Proceedings of the 2nd European Symposium on Quantitative Analysis of Microstructures in Material Science, Biology and Medicine, Caen, France*, 1978.